J Nanopart Res (2022) 24:224
https://doi.org/10.1007/s11051-022-05607-z

RESEARCH PAPER

Magnetization and optical bandgap of Cu-Mn vanadate-oxide mixed phase nanostructures

Mahmoud Mohamed Emara · **S. M. Reda** · **Mohamad Awad El-Naggar** · **Mahmoud Ahmed Mousa**

Received: 16 June 2022 / Accepted: 19 October 2022

Abstract Copper vanadate (CV) and manganese vanadate (MV) exhibit magnetic and optical properties that have drawn the attention. Due to CV polymorphism and phase multiplicity, CV is common to exist as mixed phases. In this study, nanostructures of mixed-phase CVs mixed with MV were synthesized hydrothermally followed by calcination at 400 °C, with Mn mole fractions 0.0, 0.4, 0.6, 1.0. The uncalcined and calcined Mn-Cu vanadates (MCVs) were investigated by XRD, SEM, TEM, FT-IR, EDX, ICP-AES, TGA, DTA, DSC, BET, XPS, and VSM. XRD analysis shows co-existence of multi-phase CVs with MnV_2O_6 and V oxides. Electron micrographs show nanostructures of multiple morphologies (rods, cubes, sheets, and irregular). As Mn content increased in the MCVs, their thermal stability increased, optical bandgap (E_g) declined from 2.46 to 1.60 eV, and magnetism diverted from the superparamagnetic-like to paramagnetic (H_c from 1362 to 69 G and M_r/M_s from 0.430 to 0.003). Magnetism parameters of calcined MCVs were more labile to Mn content variation compared to the uncalcined MCV counterparts.

Keywords Vanadate · Mixed oxides · Thermal stability · Band gap · Magnetism · Magnetisation · Superparamagnetic · Paramagnetic · Nanocomposites

Abbreviations

BET	Brunauer–Emmett–Teller
Δ	Difference in binding energy
cCV	Calcined Cu vanadate
cMCV4	Calcined 0.4-Mn/0.6-Cu vanadate
cMCV6	Calcined 0.6-Mn/0.4-Cu vanadate
cMV	Calcined Mn vanadate
CV	Cu vanadate
DRS	Diffuse reflectance spectroscopy
DSC	Differential scanning calorimetry
DTA	Differential thermal analysis
EDX	Electron dispersive X-ray spectroscopy
E_g	Bandgap energy
eV	Electronvolt
FT-IR	Fourier transform infrared spectrum
O_e	Oersted
M_s	Saturation magnetization
MCV4	0.4-Mn/0.6-Cu vanadate
JCPDS	Joint Committee on Powder Diffraction Standards
H_c	Coercivity
hυ	Photon energy

Supplementary Information The online version contains supplementary material available at https://doi.org/10.1007/s11051-022-05607-z.

M. M. Emara (✉)
Chemistry Department, Faculty of Science, Alexandria University, Baghdad Street, Moharam Bey, 21511 Alexandria, Egypt
e-mail: mahmoud.emara@alexu.edu.eg

S. M. Reda · M. A. El-Naggar · M. A. Mousa
Chemistry Department, Faculty of Science, Benha University, Benha, Egypt

Published online: 02 November 2022

ICP-AES	Inductively coupled plasma-atomic emission spectroscopy
MCV6	0.6-Mn/0.4-Cu vanadate
MCV	Manganese-copper vanadate
M_r	Retentivity
MV	Mn vanadate
RT	Room temperature
SEM	Scanning electron microscopy
TEM	Transmission electron microscopy
TGA	Thermal gravimetric analysis
VSM	Vibrating sample magnetometer
x_{Mn}	Mn precursor mole fraction concerning Cu + Mn
XPS	X-ray photoelectron spectroscopy
XRD	X-ray diffraction
α	Absorption coefficient

Introduction

Transition metal divanadates (MV_2O_6 or $M(VO_3)_2$, M is a transition metal) have received great interest due to their application in various fields. Specifically, CuV_2O_6 nanoparticles have been applied in supercapacitors [1], batteries [2], photocatalytic water remediation [3], photoelectrochemical sensing [4], and photoelectrochemical catalysis [5]. Specifically, copper vanadate (CV) exhibits polymorphism and phase multiplicity, and takes the formulas CuV_2O_6, α-$Cu_2V_2O_7$ (Blossite), β-$Cu_2V_2O_7$ (Ziesite), $Cu_3V_2O_8$ (Pseudolynsite), γ-$Cu_3V_2O_8$ (McBirneyite), $Cu_5V_2O_{10}$, $Cu_{11}V_6O_{26}$ (Fingerite), and $Cu_3(OH)_2V_2O_7.(H_2O)_2$ (Volborthite) [6]. Interestingly, the different CV phases can be viewed as mixtures of CuO with V_2O_5 in different ratios and mole fractions, as shown in Fig. 1 [7]. CVs can be synthesized with various approaches including co-precipitation [8, 9], hydrothermal [10, 11], thermal decomposition [6, 12], and solution combustion [7, 13].

Slight perturbation in the synthesis conditions leads to switching from one CV phase to another. Sometimes obtaining one pure phase can be a challenging task and just mixed-phase CVs originate [13–17]. The resulting mixed phases not only contain copper vanadates, but in some cases vanadium oxide may emerge as a distinct phase amongst the rest of the mixture. Hossain et al. and Keerthana et al. reported co-existence of V_2O_5 alongside with α-$Cu_2V_2O_7$ as a result of solution-combustion synthesis [3, 7].

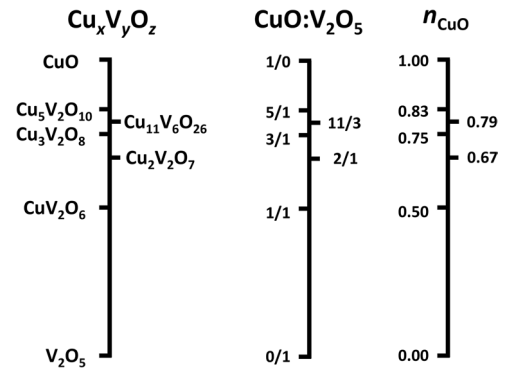

Fig. 1 The different copper vanadate phases ($Cu_xV_yO_z$) viewed as mixtures of CuO with V_2O_5 in different ratios ($CuO:V_2O_5$) and CuO mole fractions (n_{CuO}) [7]

Mixed-phase CVs have been synthesized, studied, and applied in various applications, such as photocatalytic water treatment [3], photoelectrocatalytic water treatment [13, 16], photoelectrocatalytic O_2 generation [18], photoelectrocatalytic water splitting [15]. Despite the controversy that may arise from the polymorphism and phase multiplicity of CVs, they have been pivotal in the aforementioned photoactivity-based studies, due to their visible-light absorptivity (E_g 1.80–2.74 eV) [19], and magnetism investigations [20–26].

The present work aims to study the magnetization and optical bandgap of mixed-phase nanostructures of CVs with monoclinic Mn vanadate. As well as CVs, MnV_2O_6 exhibits visible-light photoactivity [27, 28] and magnetic properties [29–33]. The proposed Mn-Cu vanadate mixed-phase (MCV) was synthesized hydrothermally followed by calcination, with Mn mole fractions $\left(x_{Mn} = \frac{Mn}{Cu+Mn}\right)$ of 0.0, 0.4, 0.6, 1.0. The investigated characteristics of the MCVs included their crystal structure, morphology, thermal stability, surface area, optical bandgap, and magnetization.

Experimental

Materials

Ammonium monovanadate extra pure (NH_4VO_3) (Oxford, India), manganese chloride tetrahydrate extra pure ($MnCl_2.4H_2O$) (Oxford, India), copper chloride

dihydrate ($CuCl_2{\cdot}2H_2O$) (Adwic Pharmaceutical and Chemicals Company, Egypt), and ethanol (C_2H_5OH) 99% (Adwic Pharmaceutical and Chemicals Company, Egypt). All chemicals and solvents were of analytical grade and used without further purification.

Hydrothermal synthesis of MCVs

MCVs of this study were synthesized according to a published method with some modifications [34]. Then, 4.8 mmol copper chloride (0.818 g) was dissolved into 80 mL of deionized water. Further, 9.6 mmol ammonium monovanadate (1.123 g) was dissolved into 80 mL deionized water at 60 °C, and then filtrated. Clear ammonium monovanadate solution was added slowly to the copper chloride solution under continuous vigorous stirring for 10 min. After the addition was completed, the resulting suspension was transferred into a 300 mL Teflon-lined stainless autoclave and maintained at 210 °C for 12 h. The autoclave was allowed to cool down to room temperature. The solid powder was collected by centrifugation, washed several times with deionized water and ethanol, and then dried at 60 °C for 4 h. The sample was labeled CV, then calcined at 400 °C for 2 h in the air (calcined sample is denoted as cCV).

Manganese vanadate was prepared by adding manganese chloride instead of copper chloride. The obtained manganese vanadate is labeled MV (before calcination) and cMV (after calcination). Mixed phases MCV4, MCV6, and their corresponding calcined samples cMCV4, cMCV6 were prepared by introducing different copper and manganese chlorides ratios as shown in Table 1.

Characterization methods and techniques

Powder x-ray diffraction (XRD) patterns were collected with BRUKER D 8 Advance, Germany. It operated with Cu Kα radiation wavelength 1.54°A, at 40 kV, 40 mA, in the diffraction angle of 2θ from 5° to 80° at a scan rate of 5° min^{-1}. The Fourier transform infrared (FT-IR) spectra of samples before and after calcination was collected by Perkin Elmer spectrum version 10.5.3 IR spectrometer in the range 4000–400 cm^{-1} at room temperature. The stoichiometric composition was obtained with inductively coupled plasma-atomic emission spectroscopy (ICP-AES) ICP-OES 5100 VDV, Agilent where 0.01 g of the MCVs after calcination were dissolved in 5 mL concentrated nitric acid then heated and completed with water to total 25 mL. Energy-dispersive X-ray spectroscopy (EDX) was conducted with field emission scanning electron microscope JEOL JSM 7000F with a 15 kV accelerating voltage. A 10 mm working distance was used to confirm the constituent elements to determine the elemental ratios. The size and morphology of the MCVs before calcination were characterized with (JEOL JEM-200CX2100F, Japan) transmission electron microscopy (TEM) with an accelerating voltage of 200 kV. Divanadate TEM samples were prepared by sonicating 0.01 g for 30 min with 5 mL of ethanol in a centrifugal tube. Cu grid 400 mesh with a thin carbon film (Quantifoil) was immersed into the dilute dispersion of samples. The morphology and microstructure of MCVs after calcination were analyzed using scanning electron microscopy (SEM) JSM-IT200. Thermal gravimetric analysis (TGA), differential thermal analysis (DTA), and differential scanning calorimetry (DSC) were carried out with SDT Q600 V20.9 Build 20; the MCV samples before calcination were put into the crucible and heated in air at a heating rate of 10 °C min^{-1} from room temperature to final temperature 800 °C. UV–vis diffuse reflectance spectroscopy (DRS) was carried out at room temperature using a PerkinElmer Lamda-900 spectrophotometer in the range of

Table 1 Amounts of Cu and Mn precursors added during the synthesis of the Cu-Mn vanadate-oxide mixed phase nanostructures. x_{Mn} is Mn mole fraction with respect to Cu + Mn

Sample	x_{Mn}	$CuCl_2.2H_2O$		$MnCl_2.4H_2O$		pH of mixed reactants
		mMol	Wt (g)	mMol	Wt (g)	
CV	0.0	4.80	0.818	0.00	0.00	4.5
MCV4	0.4	2.88	0.491	1.92	0.38	5.2
MCV6	0.6	1.92	0.327	2.88	0.57	5.6
MV	1.0	0.00	0.00	4.80	0.95	6.1

200–800 nm. Brunauer–Emmett–Teller (BET) determined the specific surface areas of MCV samples after calcination by nitrogen adsorption at 77 K using a Belsorp-mini II (Japan). Before surface area analysis, the powders were degassed at 150 °C for 3 h under vacuum. To study the surface chemistry of MCV samples after calcination, X-ray photoelectron spectroscopy (XPS) was collected with K-ALPHA (Thermo Fisher Scientific, USA) of monochromatic X-ray Al K-alpha radiation (− 10 to 1350 eV spot size 400 µm, at pressure 10–9 mbar, spectrum pass energy 200 eV, and at narrow-spectrum 50 eV). The magnetic properties of MCVs before and after calcination were measured with a vibrating sample magnetometer (VSM, Lake Shore-7410, USA) at room temperature with a magnetic field up to 20 kOe and magnetic moment sensitivity up to 1 m emu.

Results and discussion

Characterization

X-ray diffraction

Figure 2a and Table 2 of the virgin CV show peaks characteristic for three different phases. Frist, monoclinic volborthite $Cu_3(OH)_2V_2O_7{\cdot}2H_2O$ according to JCPDS Card No. 46–1443. Volborthite is a natural divanadate of formula $Cu_3(OH)_2V_2O_7{\cdot}2H_2O$ that exhibits interesting crystalline structure with porous framework [35]. As a metastable phase, Volborthite can be used as a precursor of another interesting mixed and layered crystalline phase composed of an octahedral copper-oxygen layer in coordination with tetrahedral vanadium layer. Second, monoclinic copper vanadium oxide $Cu_{0.261}V_2O_5$ according to

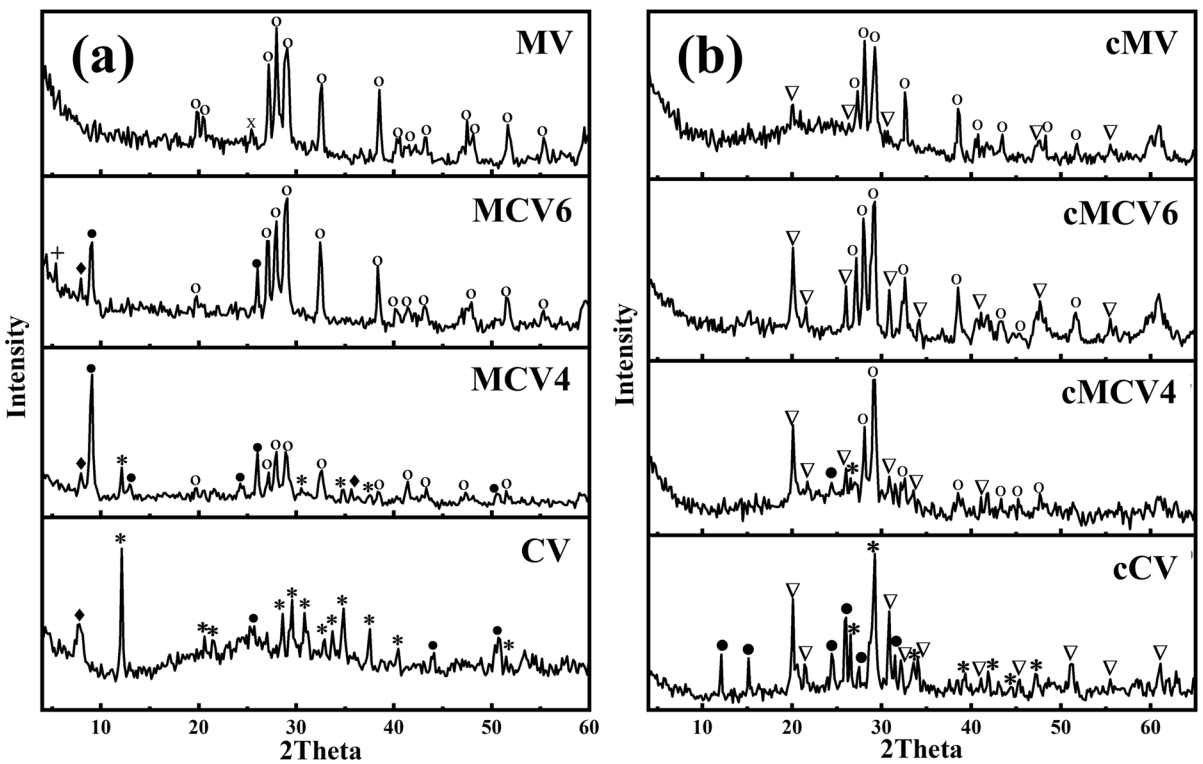

Fig. 2 **a** XRD diffractograms of the Cu-Mn vanadate-oxide mixed phase nanostructures before calcination: (asterisk) $Cu_3(OH)_2V_2O_7{\cdot}2H_2O$, (black circle) $Cu_{0.261}V_2O_5$, (black diamond) V_3O_7, (white circle) MnV_2O_6, (plus sign) $(NH_4)_8(V_{19}O_{41}(OH)_9)(H_2O)_{11}$, (multiplication sign) V_6O_{13}. **b** XRD pattern for Cu-Mn vanadate-oxide mixed phase nanostructures after calcination: (asterisk) CuV_2O_6, (black circle) $Cu_{3.64}(V_4O_{11})$, (white circle) MnV_2O_6, (down-pointing triangle) V_2O_5

JCPDS Card No. 01–079-0796. Third, a minor trace of monoclinic V_3O_7 according to JCPDS Card No. 20–1378. Two peaks observed at 2θ: 27.00 and 25.72 cannot be distinguished. In the MCV4, monoclinic MnV_2O_6 (JCPDS Card No. 35–0139) was formed beside all previous phases; $Cu_3(OH)_2V_2O_7{\cdot}2H_2O$, $Cu_{0.261}V_2O_5$, and V_3O_7. The highest noticed ratio is $Cu_{0.261}V_2O_5$ as shown from the highest sharp peak at 2θ: 9.08°. In the MCV6, the peaks characteristic for $Cu_3(OH)_2V_2O_7{\cdot}2H_2O$ disappeared, whereas the intensities of the peaks characterized for $Cu_{0.261}V_2O_5$ and MnV_2O_6 increased, besides a weak peak intensity for V_3O_7 is noticed. Ammonium vanadium oxide hydroxide hydrate, $(NH_4)_8(V_{19}O_{41}(OH)_9)(H_2O)_{11}$, exists as a trace amount with a characteristic peak at 2θ: 5.4° according to JCPDS Card No. 01–078-2016. In MV, the dominant phase is MnV_2O_6 beside a foreign peak at 2θ: 25.56°, which may be due to the presence of traces of orthorhombic V_6O_{13} according to JCPDS Card No. 778–0983.

The calcined samples in the air at 400 °C for 2 h, cCV, cMCV4, cMCV6, and cMV, show significant XRD changes than those of the virgin samples in addition to formation of new phases as shown in Fig. 2b and listed in Table 2. The XRD peaks of cCV are indexed to the $Cu_{3.64}(V_4O_{11})$ phase according to JCPDS Card No. 1–085-0226, CuV_2O_6 phase according to JCPDS Card No. 45–1054 and Shcherbinaite V_2O_5 phase according to JCPDS Card No. 9–0387. The XRD peaks of cMCV4 refer to the presence of the MnV_2O_6 phase in addition to all the previously mentioned phases: $Cu_{3.64}(V_4O_{11})$, CuV_2O_6, and V_2O_5. The XRD of cMCV6 demonstrates the presence of $Cu_{3.64}(V_4O_{11})$, V_2O_5, and MnV_2O_6 phases, while the CuV_2O_6 phase disappeared. For cMV, all the XRD peaks are indexed to MnV_2O_6 and V_2O_5.

Fourier transform infrared

FT-IR spectra analysis was performed to investigate the structure and functional groups. Figure 3a shows the FTIR spectra of the uncalcined MCV samples. The bands observed at 500–1010 cm^{-1} correspond to the metal–oxygen bonds stretching and wagging (Cu–O, Mn–O, and V–O). The band at 899–886 cm^{-1} arises from the symmetric stretching vibration of ν_1-VO_3, and that at 751 cm^{-1} is corresponding to the anti-symmetric stretching vibration of ν_3-VO_3 of CV. The two bands at 530 cm^{-1} and 509 cm^{-1} are assigned to the ν_3 symmetric and ν_1 symmetric stretching modes of (V–O–V) of CV [36]. Those at 993–1010 cm^{-1} are corresponding to $\nu(V^{4+}=O)$ [37, 38]. The band observed at 575 cm^{-1} for MV is assigned for Mn–O vibration [39]. The bands at 1401–1405 cm^{-1} are assigned to symmetric stretching of CO_2 due to the absorption of CO_2 from the air [40]. The bands at 1613–1620 cm^{-1} correspond to the ν-OH stretching vibration and δH_2O bending vibration of water molecules. The bands at 2700–3000 cm^{-1} are assigned to organic impurities on the surface of the samples (maybe resulting from handling) [41]. The bands at 3400–3600 cm^{-1} are assigned to the ν-OH stretching vibration of water molecules [36].

Figure 3b shows the FTIR spectra of the calcined MCVs. It can be noticed that plenty of the bands of the uncalcined MCVs have disappeared upon calcination due to the elimination of H_2O, CO_2, and OH groups. The bands at 400–1010 cm^{-1} correlate to metal–oxygen bonds that have become stronger by calcination. Those at 795–1024 cm^{-1} are attributed to the vibrational mode of V = O bonds. The strong bands at1016–1024 cm^{-1} represent the V = O bond in V_2O_5 as a common product in all calcined samples. This band is very small for cMV due to the dimmish of V_2O_5 [42]. The presence of the Mn–O bond could be observed at ~ 558 cm^{-1}, which is closed to that reported in the literature at 564 cm^{-1} [39, 40]. The bands at 1401–1405 cm^{-1} of CO_2 symmetric stretching disappeared completely after calcination. The intensities of vibration bands at 1613–1620 cm^{-1} of the ν-OH stretching vibration and δH_2O bending vibration of water molecules decreased due to water removal. The bands at 3000–2700 cm^{-1} are assigned to organic impurities decreased also. The bands at 3600–3400 cm^{-1} of the ν-OH stretching vibration of water molecules also disappeared due to the water elimination during the calcination process.

ICP and EDX elemental analysis

The EDX (Fig. 4) and ICP analysis show that the metals ratios (Cu, Mn, and V) are in good match with the starting concentrations of Cu^{2+}, Mn^{2+}, and VO_3^- added during the synthesis as shown in Table 3. Detailed raw EDX scan results are given in

Table 2 Based on the XRD results, phases constituting the uncalcined and calcined Cu-Mn vanadate-oxide mixed phase nanostructures, in addition to their average particle sizes estimated with the Scherrer equation. **P**: present, **M**: major and **T**: traces. JCPDS Card numbers: (**a**) 46–1443, (**b**) 01–079-0796, (**c**) 20–1378, (**d**) 35–0139, (**e**) 778–983, (**f**) 01–078-2016, (**g**) 1- 085–0226, (**h**) 9–0387 and (**i**) 45–1054

Phase	CV	MCV4	MCV6	MV
$Cu_3(OH)_2V_2O_7{\cdot}2H_2O$ [(a)]	P	P	–	–
$Cu_{0.261}V_2O_5$ [(b)]	P	P	P	–
V_3O_7 [(c)]	T	P	P	–
MnV_2O_6 [(d)]	–	P	P	M
V_6O_{13} [e]	–	–	–	T
$(NH_4)_8(V_{19}O_{41}(OH)_9)(H_2O)_{11}$ [(f)]	–	–	T	–
Average D_{Sch} (nm)	25	15	19	20
Phase	cCV	cMCV4	cMCV6	cMV
$Cu_{3.64}(V_4O_{11})$ [(g)]	P	P	P	–
V_2O_5 [(h)]	P	P	P	T
CuV_2O_6 [(i)]	P	P	–	–
MnV_2O_6 [(d)]	–	P	P	M
Average D_{Sch} (nm)	13	20	19	27

Figs. S1, S2, S3, and S4 in the supplementary information for samples cCV, cMCV4, cMCV6, and cMV, respectively.

Morphology of the uncalcined and calcined copper/manganese vanadates by scanning and transmission electron microscopy

Figure 5 is the TEM micrographs of the synthesized MCVs before calcination. CV shows nanowire bundles with several micrometers in length and cubic nanostructures of an average size of 100–300 nm. MCV4 shows nanowires with a slight increase in diameter (around 50 nm), cubic structures, and nanosheets (around 500 nm size). Since MV TEM images show all nanosheets only, these nanosheets are assumed to be of the MnV_2O_6 phase. MCV6 shows an increase in the abundance of MnV_2O_6 nanosheets and the thickness of nanowires, while absence of the cubic structures. MV shows MnV_2O_6 nanosheets of different sizes.

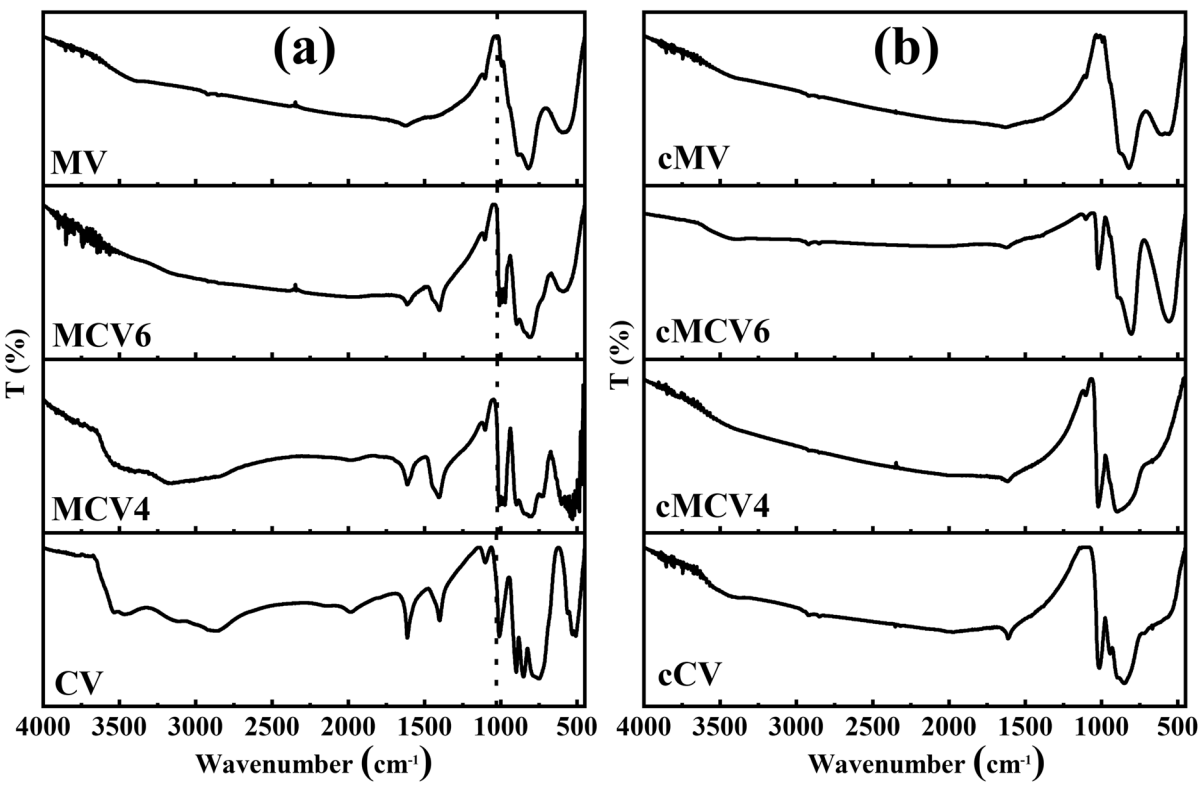

Fig. 3 FTIR spectra of Cu-Mn vanadate-oxide mixed phase nanostructures before **a** and after **b** calcination

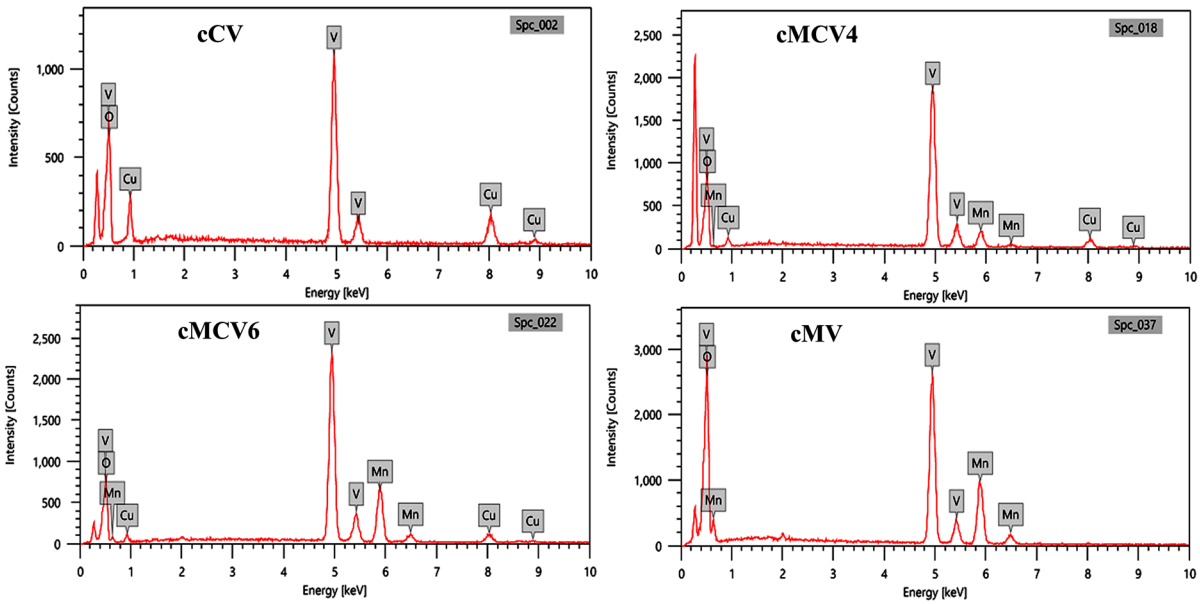

Fig. 4 EDX qualitative and quantitative detection of Cu, Mn, V, and O in the calcined Cu-Mn vanadate-oxide mixed phase nanostructures

Figure 6 shows SEM micrographs of cMCVs. cCV consists of nano-rods beside irregular shapes. This may be attributed to the presence of muli-phases of copper vanadates and V_2O_5. In cMCV4, shapes are more irregular, while in cMCV6, sheets the abundance with fewer rods than cCV. In cMV, there are no rods, and the sample is all nanosheets either stacked or separate.

Table 3 The Cu, Mn, and V elemental ratios according to the ICP and XPS techniques, in addition to the specific surface area, average pore volume, and pore diameter according to the BET technique, all for the calcined Cu-Mn vanadate-oxide mixed phase nanostructures. (*) The ideal stoichiometric ratio of V/(Cu + Mn) based on the expected formula MV_2O_6 should be 2, as shown in the brackets. (#) According to the added ratios during the synthesis, x was expected to change as 0.00, 0.40, 0.60, and 1.00 for samples cCV, cMCV4, cMCV6, and cMV, respectively, as shown in the brackets

	cCV	cMCV4	cMCV6	cMV
ICP				
Cu	0.27	0.13	0.06	0.00
Mn	0.00	0.08	0.19	0.34
V	0.73	0.79	0.75	0.66
V/(Cu + Mn) *	2.70 (2.00)	3.76 (2.00)	3.00 (2.00)	1.94 (2.00)
x = Mn/(Mn + Cu) #	0.00 (0.00)	0.38 (0.40)	0.76 (0.60)	1.00 (1.00)
XPS				
Cu	0.25	0.06	0.04	0.00
Mn	0.00	0.04	0.04	0.16
V	0.75	0.90	0.92	0.84
V/(Cu + Mn) *	3.00 (2.00)	9.00 (2.00)	11.50 (2.00)	5.25 (2.00)
x = Mn/(Mn + Cu) #	0.00 (0.00)	0.40 (0.40)	0.50 (0.60)	1.00 (1.00)
BET				
S_{BET} (m^2/g)	4.7	8.6	5.4	1
Pore volume (cm^3/g) × 10^{-2}	6.13	11.60	7.96	2.30
Main Pore diameter (nm)	52.3	53.9	59.4	92.7

Thermogravimetric analysis of copper and manganese vanadates (TGA, DTA, and DSC)

Figure 7 and Table 4 show the thermal analyses of the uncalcined MCVs carried out under an air atmosphere at a heating rate of 10 °C/min from the ambient temperature to 800 °C. The weight losses observed in the TG thermograms (Fig. 7a) are generally due to the removal of adsorbed water, crystallization water, and hydroxyl groups. The results are summarized in Table 4. For CV, the loss in weight takes place at four stages: the first stage starts from ambient temperature to 175 °C, the weight loss is 5.5% which may be due to the removal of adsorbed water and some crystallization water of the Volborthite phase. In the second stage, starting from 175 to 260 °C, the weight loss is 4.8% which is attributed to the complete removal of crystalline water of volborthite. In the third stage, starting from 260 to 400 °C, the weight loss is 3.9% due to removing two hydroxyl groups of Volborthite [43, 44]. The TG curve also shows another weight loss started at about 635 °C, which corresponds to the melting point of CuV_2O_6 in the CV sample. An endothermic peak accompanying this step appeared in each DTA and DSC thermogram (Fig. 7b and c). In the MCV4 sample, the weight loss of the melting step started at about 698 °C due to the melting point of V_2O_5 [45]. With decreasing the ratio of copper in the investigated samples, the weight loss also decreases since the samples contain fewer phases of crystallization water and hydroxyl groups (as pointed out in the XRD analysis and Table 2). MV exhibits minimal weight loss, which may be due to its phase stability and it shows only phase of MnV_2O_6 all over the thermal treatment.

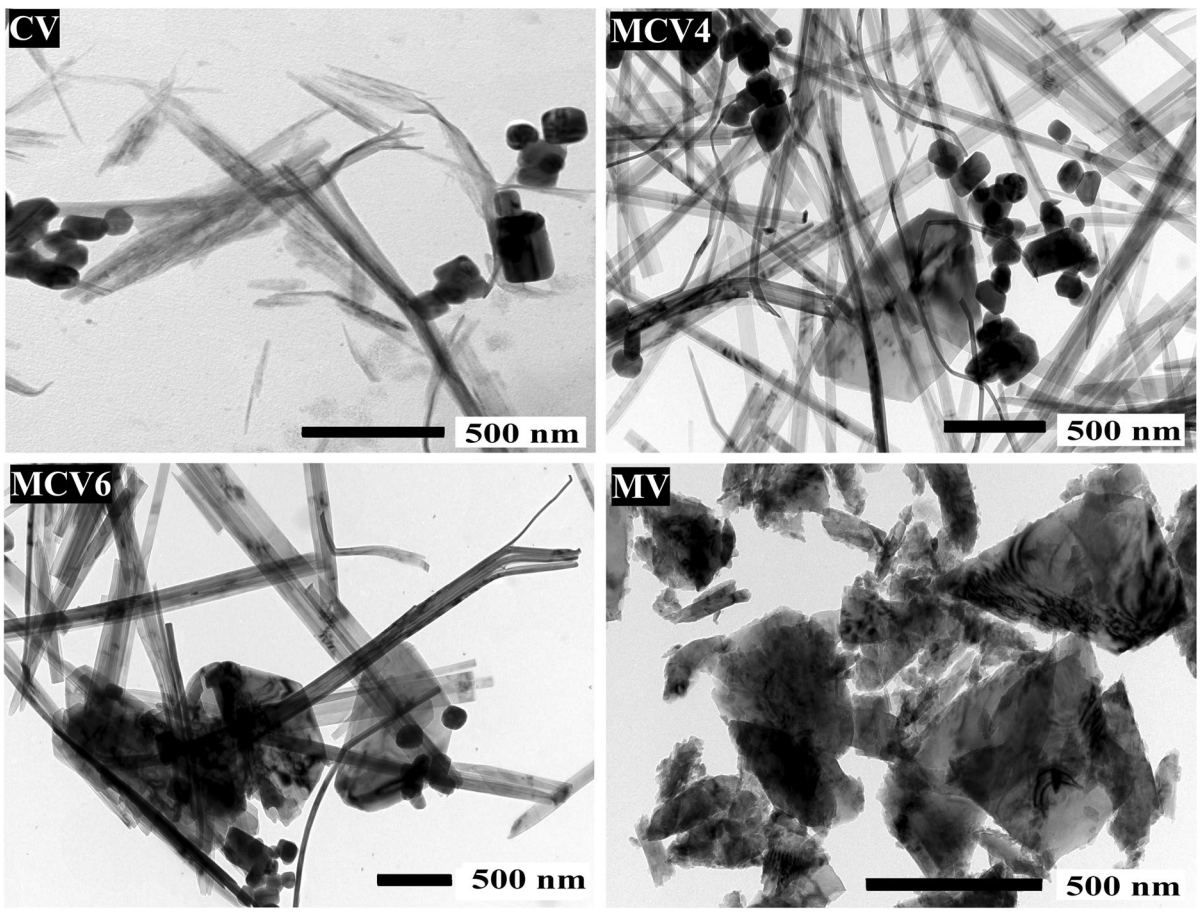

Fig. 5 TEM images of the uncalcined Cu-Mn vanadate-oxide mixed phase nanostructures

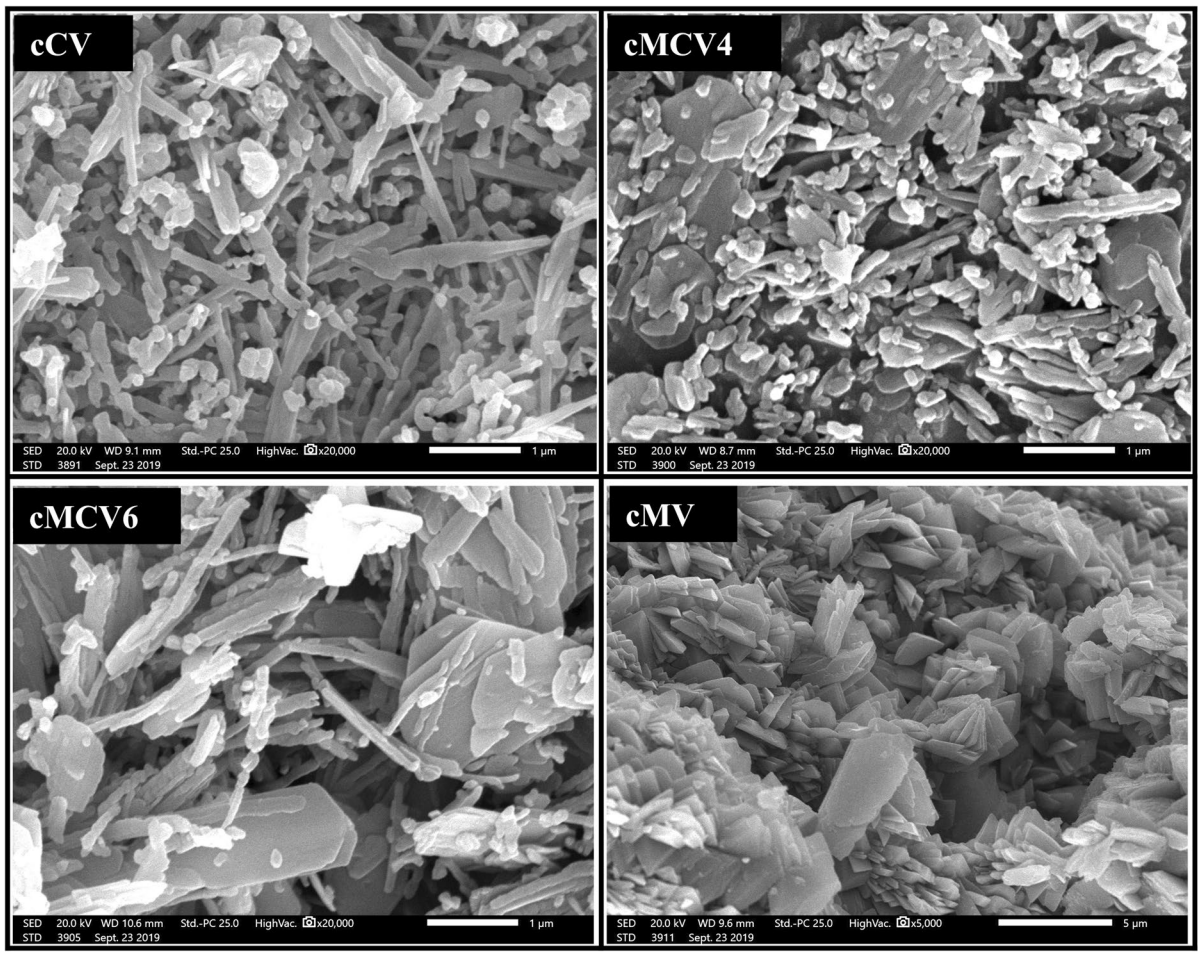

Fig. 6 SEM images of the calcined Cu-Mn vanadate-oxide mixed phase nanostructures. The scale bar is equivalent to 1 µm

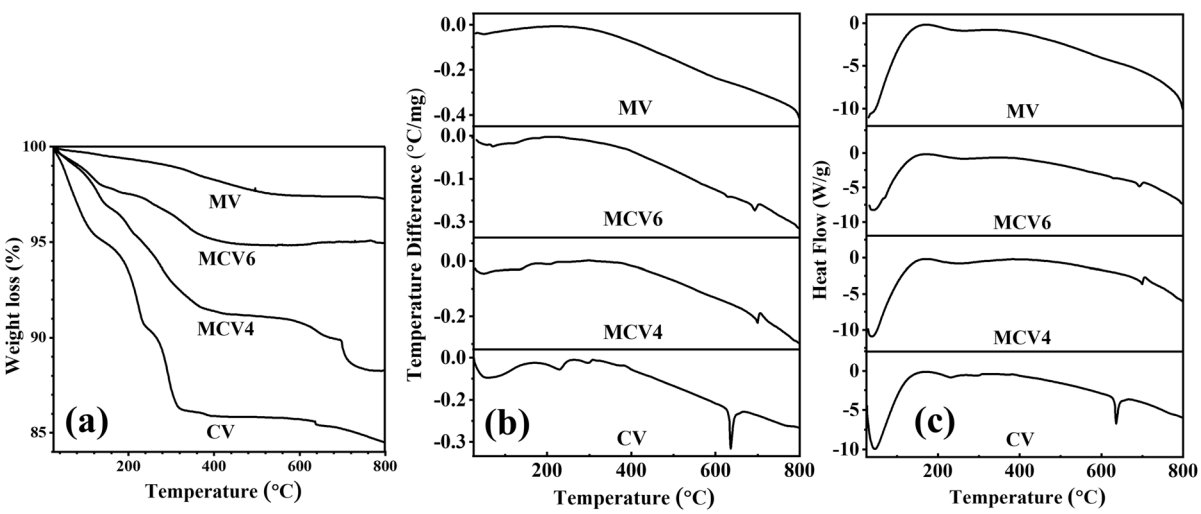

Fig. 7 Plots of TG (**a**), TDA (**b**), and DSC (**c**) of the uncalcined Cu-Mn vanadate-oxide mixed phase nanostructures

Table 4 Thermogravimetric data of uncalcined Cu-Mn vanadate-oxide mixed phase nanostructures

	Temperature (°C)	Weight loss (%)	Significance
CV	27–175	5.5	Removing adsorbed water, besides the elimination of crystallized water molecules
	175–260	4.8	
	260–400	3.9	
	635–800	1.3	
MCV4	27–170	3.4	Removing adsorbed water, besides the elimination of crystallized water molecules
	170–390	5.1	
	390–600	0.7	
	600–698	0.9	
	698–760	1.7	
MCV6	27–175	2.3	Removing adsorbed molecules
	175–410	2.7	
MV	27–550	2.5	Removing adsorbed water

Optical bandgap by diffuse reflectance spectroscopy

The optical spectra of the MCVs, before and after calcination, are shown in Fig. 8a and b. All MCVs show two absorption peaks; a small one at the UV range and broadband in the visible region. The results are summarized in Table 5. The bands that appeared in UV and visible regions are attributed to several phases of copper vanadates accompanying MnV_2O_6 and V_2O_5. The optical bandgaps of the MCVs in the visible region were determined using Tauc equation as shown in Fig. 8c and d.

$$(\alpha h\upsilon)^n = B(h\nu - E_g) \quad (1)$$

where hυ is the photon energy (E_{photon}), α is the absorption coefficient, is a proportionality constant, and "n" depends on the type of transition, $n = 1/2$ for direct transmission, and $n = 2$ for indirect transmission [46]. The bandgap energy (E_g) was determined by extrapolating the linear part of $(\alpha h\nu)^2$ vs. $h\nu$ plot to intercept the horizontal E_{photon} axis as shown in Fig. 8c and d. The calculated E_g values for calcined and uncalcined MCVs are given in Table 5 and plotted versus x_{Mn} in Fig. 8e. In both uncalcined and calcined MCVs, E_g declined with the increase of x_{Mn}, whereas the uncalcined ones were more responsive.

Specific surface area by BET

The N_2 adsorption–desorption isotherms, as shown in Fig. 9, are identified as V type, which exhibits low adsorption at low gas pressure, indicating relatively weak affinity between gas and solid [47]. The sharply upward hysteresis loops of the samples close to $P/P_0 = 1$ suggest that the adsorption occurs in micropores and/or mesopores, where the interactions between the adsorbent and the adsorbate are relatively weak. The surface data of the specimens investigated are listed in Table 3. The surface area increases in the sequence cMCV4 > cMCV6 > cCV > cMV. The minimal surface area of cMV is attributed to the nanosheet structure, which is subject to stacking. One the other hand, cMCV4 and cMCV6 act show maximal surface area, probably due to the multiplicity of their phase composition. The pore size exhibits a broad range within 52–93 nm. These results further confirm the presence of macropores [48].

X-ray photoelectron spectroscopy

The XPS spectra of cCV, cMCV4, cMCV6, and cMV, and their analysis are given in Fig. 10 and Table 6, respectively. The figure shows the presence of Cu, Mn, V, and O, and absence of any other foreign elements referring to the purity of the samples, which is further confirmed via XRD, FTIR, ICP, and EDX techniques. Due to the spin–orbit coupling, there are peaks for $2p^{1/2}$ at lower energy than those of $2p^{3/2}$, for each of Cu, Mn, V. Each of the three elements exist in the samples in two oxidation states, one higher than the other, which result in two peaks under each of $2p^{1/2}$ and $2p^{3/2}$. However, the high and low valency peaks tend to overlap and hide under the parent peaks of $2p^{1/2}$ and $2p^{3/2}$, and in order to show them in high resolution, those peaks are deconvoluted by the XPS peak differentiation-imitation method. The peak at ~ 284.8 eV is characterized by C 1 s (called adventitious carbon) and originates from the adventitious contamination layer [49]. C 1 s peak

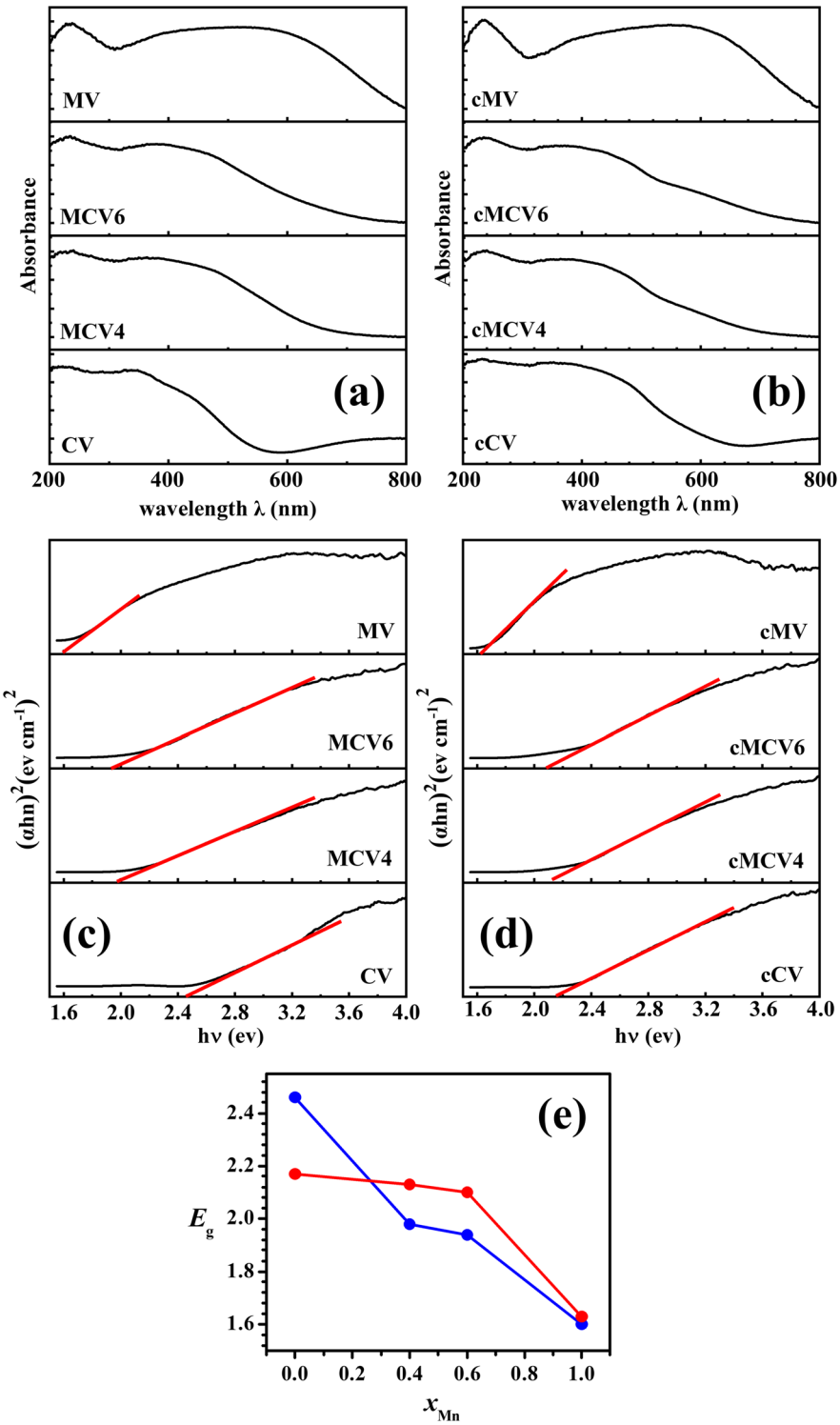

Fig. 8 UV–vis absorption spectra of the Cu-Mn vanadate-oxide mixed phase nanostructures, before (**a**) and after (**b**) calcination. The Tauc plots $[(\alpha h\nu)^2$ vs. $h\upsilon]$ before (**c**) and after (**d**) calcination. Dependence of bandgap of the uncalcined MCVs (blue curve in inset **e**) and calcined MCVs (red curve in inset **e**) on x_{Mn}

is used as a reference to obtain the exact peaks values [50, 51]. The intensity of the carbon peak increased as the amount of time spent inside the instrument increased [52].

Table 5 Absorption peaks wavelengths in the UV and visible spectra as well as E_g values of the uncalcined and calcined Cu-Mn vanadate-oxide mixed phase nanostructures

	CV	MCV4	MCV6	MV
UV peaks (nm)	215	240	234	238
Visible peaks (nm)	380	382	380	516
Band gap (E_g) (eV)	2.46	1.98	1.94	1.60
	cCV	cMCV4	cMCV6	cMV
UV peaks (nm)	232	240	235	237
Visible peaks (nm)	380	348	380	545
Band gap (Eg) (eV)	2.17	2.13	2.10	1.63

XPS spectra of Cu^{2+} have characteristic satellite peaks, which are prominent at 940.7, 943.3, 961.7 eV; these satellite peaks are characteristic of materials having ground-state d^9 configuration, i.e., Cu^{2+} [53, 54]. The binding energy difference between $2p^{3/2}$ and $2p^{1/2}$ is 19.95 eV, which is close to the literature slandered value [55, 56]. The molar ratio between Cu^{1+} and Cu^{2+} are nearly given Table 6, based on $2p^{1/2}$ peaks analysis. In the manner of Cu analysis, Mn shows 2 main peaks ($2p^{3/2}$ and $2p^{1/2}$) and each of them is deconvoluted to two sub-peaks for Mn^{2+} and Mn^{3+} [57, 58]. The table also shows the molar ratio between Mn^{2+} and Mn^{3+} according to the $2p^{1/2}$ peaks analysis. The peaks appearing around 516.3–516.78 eV and 521.99–524.32 eV are assigned to the V $2p^{3/2}$ and $2p^{1/2}$. Due to the multivalency of V (V^{3+}, V^{4+}, and V^{5+}), multiple sub-peaks appear in the deconvolution of the high resolution [59–62]. The second highest-binding-energy peak is found at 531.53 eV (perhaps a third peak at 533.00 eV). The O 1 s XPS signals are divided into three peaks for cCV, cMCV6, cMV, and four peaks for cMCV4. The prominent peak in all samples has binding energy in the range of 529.09–529.93 eV, which is usually for lattice O of several spinel 3d metal oxides [63]. However, the exact assignment of the higher binding energy peaks is somewhat complex and controversial as numerous factors like surface defects, contaminants, impurities, or chemisorbed oxygen species could result in the appearance of shoulder peaks [64, 65].

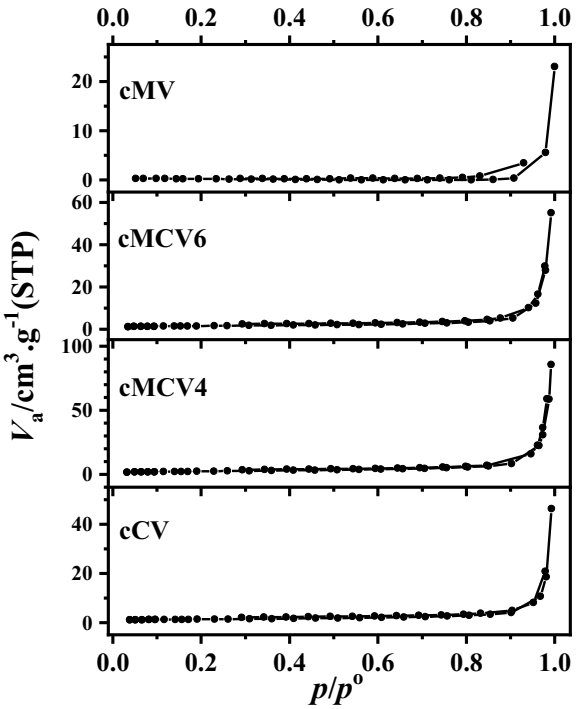

Fig. 9 N_2 adsorption/desorption BET isotherms of the calcined Cu-Mn vanadate-oxide mixed phase nanostructures

Magnetic properties

Figure 11 shows the M-H magnetization of the uncalcined and calcined MCVs under the influence of an external magnetic field at room temperature, and Table 7 summarizes their magnetism parameters. Figure 12 represents the impact of x_{Mn} on the various magnetism parameters, including coercivity field (H_c), magnetization saturation (M_s), remanent magnetization (M_r), and remanence ratio (M_r/M_s).

According to Fig. 12, all four parameters are more responsive to the Mn/Cu ratio in the calcined MCVs than in their uncalcined counterparts. Furthermore, with the increase of Mn, both H_c and M_s seem to change linearly in the uncalcined samples, while the former declines and the later rises. M_r does not show a remarkable response to the variation in x_{Mn} in the uncalcined MCVs. In the calcined MCVs, all of H_c, M_r, and M_r/M_s decrease remarkably with the increase of x_{Mn}, unlike M_s, which increases. At $x_{Mn} > 0.6$ in the calcined MCVs, none of H_c, M_r, or M_r/M_s is responsive to the changes in x_{Mn}. As x_{Mn} increased, the MCVs tend to divert from the superparamagnetic-like to paramagnetic (especially the calcined), where the uncalcined H_c declined from 396 to 118 G and M_r/M_s from 0.110 to 0.006 and for the calcined from 1362 to 69 G and from 0.430 to 0.003, respectively.

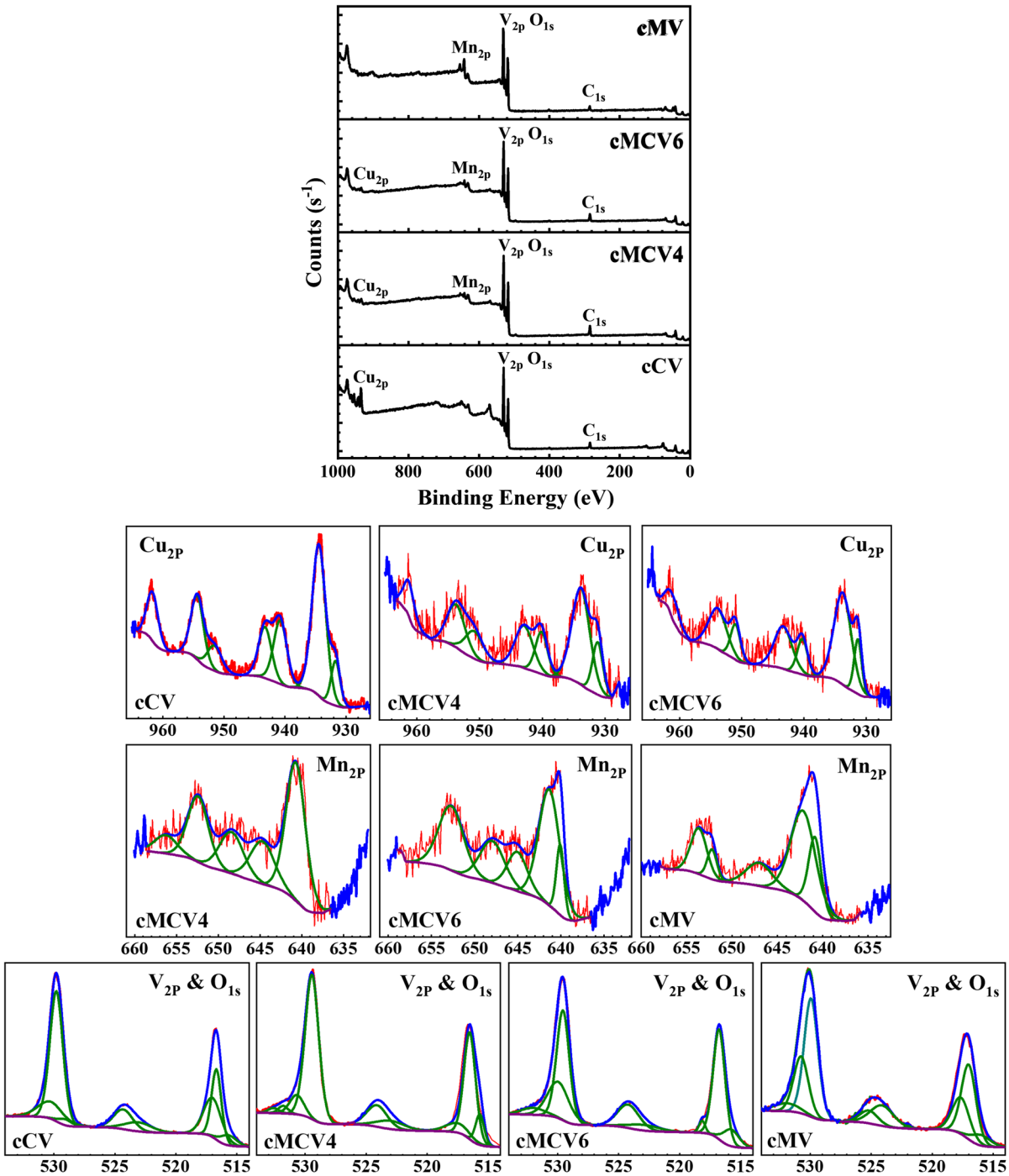

Fig. 10 XPS survey scans for the calcined Cu-Mn vanadate-oxide mixed phase nanostructures (top panel) and their corresponding Cu, Mn, V, and O high-resolution peaks (the bottom 10 panels)

The magnetic characteristics of the studied materials depend on the magnetic interaction (superexchange interaction) between metal ions with magnetic moments in the crystal lattice. Thus,

VSM studies were performed at room temperature within − 20 kOe to + 20 kOe. As shown in Fig. 11 and 12, the uncalcined MCVs show weak hysteresis with a very small magnetic coercivity at a low magnetic field, indicating superparamagnetic-like behavior. The value of magnetic coercivity of the uncalcined MCVs follows the order: CV > MCV4 > MCV6 > MV, as shown in Table 7 and Fig. 12.

It is noted that all the studied MCVs did not reach complete saturation even under a high magnetic field of 20 kOe. Several authors have reported the reduction of magnetization in NPs and proposed mechanisms to explain the no-saturation behavior in a high magnetic field. It can be attributed to the presence of a spin disordered surface layer, which requires a larger magnetic field to reach saturation magnetization [66]. The saturation magnetization (estimated from the linear extrapolation of M vs. $1/H$ plot) of all samples is listed in Table 7. The chemical composition can significantly influence the magnetization behavior because of changes in the distribution of cations and the particle size. The reduction of the magnitude of magnetization is ascribed to the noncollinear spin arrangement at the particle surface and the difference in the magnetization characteristic of two sub-lattices due to cation redistribution [67]. The disordered or misaligned surface spins weaken the total magnetization of the material NPs, with small retentivity and coercivity values. These values indicate that the thermal variations are enough to dominate the anisotropic energy barrier of the studied samples and reverse the magnetization direction spontaneously. As seen in Table 7 and Fig. 12, the retentivity (M_r) and coercivity (H_c) values show variation concerning sample composition, which can be attributed to the interaction among the oxygen and metal ions in the sublattice of the crystals.

Conclusion

Due to CV polymorphism and phase multiplicity, the Cu, Mn, and V stoichiometry in the MCVs did not follow the metal divanadate formula MV_2O_6 (M = Cu or Mn) nor did it follow the precursor Mn mole fraction $x_{Mn} = \frac{Mn}{Cu+Mn} = 0.0, 0.4, 0.6, 1.0$. The $\frac{V}{Cu+Mn}$ ratio reached as high as 3.0–11.5, while it was expected to

Table 6 XPS-based core-electrons binding energies (eV) of Cu, Mn, V, and O constituents in the calcined Cu-Mn vanadate-oxide mixed phase nanostructures

	cCV	cMCV4	cMCV6	cMV	References
Cu					
$2p^{3/2}$	931.68 (Cu^{1+}) 934.41 (Cu^{2+})	931.18 (Cu^{1+}) 933.86 (Cu^{2+})	931.33 (Cu^{1+}) 933.78 (Cu^{2+})	–	[53–56]
2p½	951.52 (Cu^{1+}) 954.36 (Cu^{2+})	950.85 (Cu^{1+}) 953.76 (Cu^{2+})	951.01 (Cu^{1+}) 953.86 (Cu^{2+})	–	
Satellite peaks	940.74, 943.26, 961.7	940.14, 942.92,961.22	940.26, 943.35, 961.06	–	
Cu^{1+}:Cu^{2+}	0.16:0.84	0.24:0.76	0.21:0.79		
Mn					
$2p^{3/2}$	–	640.73 (Mn^{2+})	640.08 (Mn^{2+}) 641.33 (Mn^{3+})	640.83 (Mn^{2+}) 642.12 (Mn^{3+})	[57, 58]
2p½	–	652.41 (Mn^{2+}) 656.27 (Mn^{3+})	652.71 (Mn^{2+})	652.44 (Mn^{2+}) 653.30 (Mn^{3+})	
Satellite peaks	–	644.72, 648.42	645.04, 647.96	646.99	
Mn^{2+}:Mn^{3+}		1.00:0.00	0.18:0.82	0.29:0.71	
V					
$2p^{3/2}$	516.3, 516.66, 516.74	516.43, 516.44, 516.62	516.33, 516.6, 516.78	516.77, 516.99, 517.64	[59–62]
2p½	523.09, 524.32	523.00, 524.12	522.91, 524.22	521.99, 524.11, 525.19	
O					
1S	529.09, 529.79, 530.24	529.45, 530.69, 531.8, 532.59	529.57, 529.95, 532.03	529.93, 530.75, 531.9	

be only 2 if it followed the divanadate formula MV_2O_6.

Regardless of the precursor Cu and Mn mole fractions and regardless of the post-synthesis thermal treatment, each MCV sample consisted of 2–4 different vanadate-oxide phases of $(NH_4)_8(V_{19}O_{41}(OH)_9)(H_2O)_{11}$, V_2O_5, V_3O_7, V_6O_{13}, $Cu_3(OH)_2V_2O_7{\cdot}2H_2O$, $Cu_{0.261}V_2O_5$, $Cu_{3.64}(V_4O_{11})$, CuV_2O_6, or MnV_2O_6. When there was no copper, vanadium oxide was a trace phase accompanying the major phase of MnV_2O_6. Phase multiplicity of the MCVs clearly appears in the electron micrographs, where particles morphology in each MCV varies between nanowires, bundles of nanowires, nanocubes, nanosheets, and irregular structures.

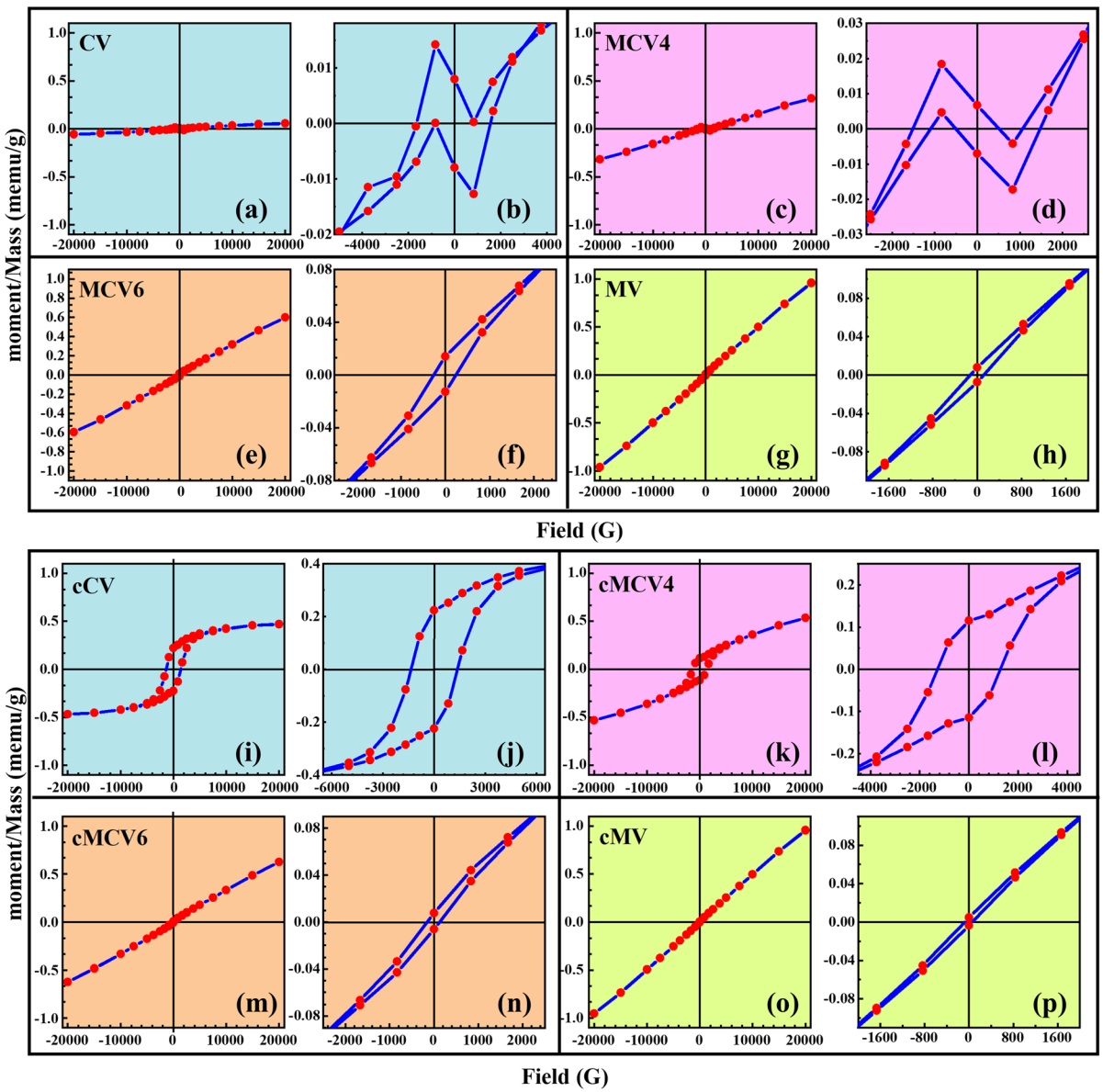

Fig. 11 M–H magnetization plots of the uncalcined Cu-Mn vanadate-oxide mixed phase nanostructures (insets **a**–**h**) and the calcined ones (insets **i**–**p**). Plots **b**, **d**, **f**, **h**, **j**, **l**, **n**, and **p** are zoomed-in M-H plots for clarification of the hysteresis behavior

Table 7 Magnetism parameters of the uncalcined and calcined Cu-Mn vanadate-oxide mixed phase nanostructures

	CV	MCV4	MCV6	MV
H_c (G)	396	272	249	118
M_s (emu/g)	0.07	0.42	0.77	1.24
M_r (emu/g × 10^{-3})	8.0	6.9	13.0	7.6
M_r/M_s (× 10^{-3})	110	17	15	6
	cCV	cMCV4	cMCV6	cMV
H_c (G)	1362	1277	140	69
M_s (emu/g)	0.51	0.65	0.80	1.23
M_r (emu/g × 10^{-3})	220	110	7	4
M_r/M_s (×10^{-3})	430	170	9	3

As Mn content increased, the uncalcined MCVs showed more thermal stability and their optical bandgap remarkably declined. The calcined MCVs showed less bandgap response to the Mn-content variation than the uncalcined ones, although they all lay within 1.60–2.46 eV (all visible).

The uncalcined MCVs tend to divert from the superparamagnetic-like to be paramagnetic with the increase of Mn content, since both H_c and M_s seem to linearly decline and rise, respectively. This behavior is more evident in the calcined MCVs, where all of H_c, M_r, and M_r/M_s decrease remarkably with the increase of x_{Mn}, unlike M_s, which increases.

Acknowledgements Not applicable.

Author contribution Mahmoud Mohamed Emara: conceptualization, data curation, formal analysis, investigation, methodology, project administration, resources, software, supervision, validation, writing—original draft, writing—review and editing. S. M. Reda: conceptualization, project administration, resources, supervision, writing—original draft, writing—review and editing. Mohamad Awad El-Naggar: conceptualization, data curation, formal analysis, funding acquisition, investigation, methodology, resources, software, validation, writing—original draft, writing—review and editing. Mahmoud Ahmed Mousa: conceptualization, data curation, formal analysis, investigation, methodology, project administration, resources, software, supervision, validation, writing—original draft, writing—review and editing.

Funding Open access funding provided by The Science, Technology & Innovation Funding Authority (STDF) in cooperation with The Egyptian Knowledge Bank (EKB).

Data availability The datasets used and/or analyzed during the current study are available from the corresponding author on reasonable request.

Prime novelty statement All data and work included in this paper are original and have not been published or

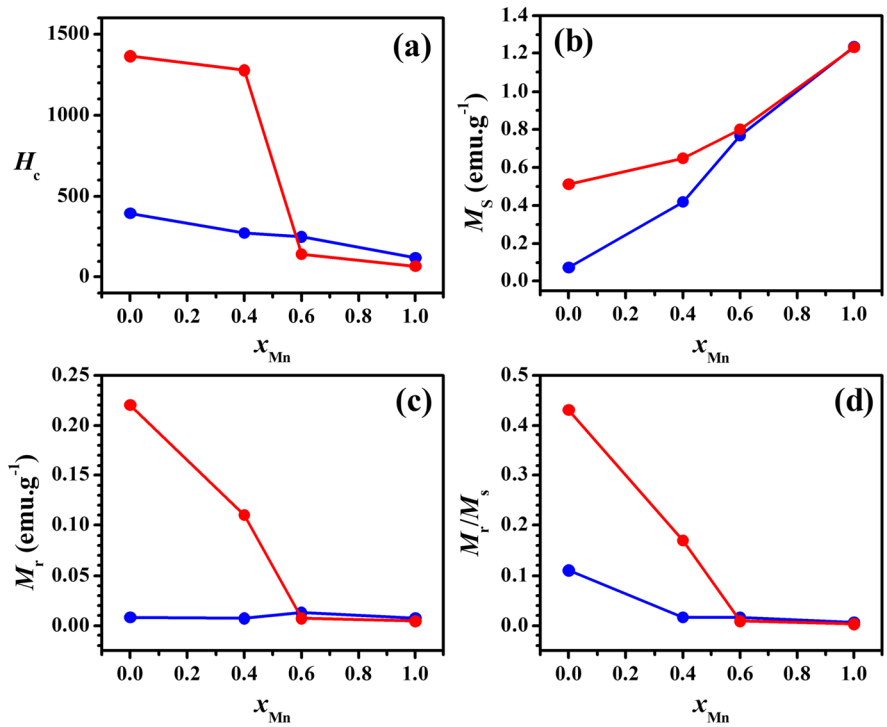

Fig. 12 Plots of various magnetism parameters H_{ci} **(a)**, M_s **(b)**, M_r **(c)**, and M_r/M_s **(d)** versus Mn molar ratio in the synthesis precursors added during the synthesis of the Cu-Mn vanadate-oxide mixed phase nanostructures. The blue and red curves represent the uncalcined and calcined samples, respectively

under consideration of publishing by any other periodical or publisher.

Declarations

Competing interests The authors declare no competing interests.

References

1. Barik R, Barik G, Tanwar V, Ingole PP (2022) Supercapacitor performance and charge storage mechanism of brannerite type CuV2O6/PANI nanocomposites synthesis with their theoretical aspects. Electrochim Acta 410:140015. https://doi.org/10.1016/j.electacta.2022.140015
2. Song J et al (2022) Freestanding CuV2O6/carbon nanotube composite films for flexible aqueous zinc-ion batteries. Appl Surf Sci 578:152053. https://doi.org/10.1016/j.apsusc.2021.152053
3. Keerthana SP, Yuvakkumar R, Kumar PS, Ravi G, Velauthapillai D (2022) Surfactant induced copper vanadate (β-Cu2V2O7, Cu3V2O8) for different textile dyes degradation. Environ Res 211:112964. https://doi.org/10.1016/j.envres.2022.112964
4. Dong B, Sun T, Jiang X, Guo P, Yang G, Wang F (2021) Self-passivated CuV2O6 as a universal photoelectrode material for reliable and accurate photoelectrochemical sensing. Chem Commun 57(60):7402–7405. https://doi.org/10.1039/D1CC02891J
5. Oliveira JA et al (2022) Copper vanadates: targeted synthesis of two pure phases and use in a photoanode/cathode setup for selective photoelectrochemical conversion of carbon dioxide to liquid fuel. Mater Res Bullet 149:111716. https://doi.org/10.1016/j.materresbull.2021.111716
6. Yamuna A, Chen T-W, Chen S-M, Jiang T-Y (2021) Facile synthesis of single-crystalline Fe-doped copper vanadate nanoparticles for the voltammetric monitoring of lethal hazardous fungicide carbendazim. Microchim Acta 188(8):277. https://doi.org/10.1007/s00604-021-04941-8
7. Hossain MK et al (2020) Phase-pure copper vanadate (α-CuV2O6): solution combustion synthesis and characterization. Chem Mater 32(14):6247–6255. https://doi.org/10.1021/acs.chemmater.0c02227
8. Wei YJ, Nam KW, Chen G, Ryu CW, Kim KB (2005) Synthesis and structural properties of stoichiometric and oxygen deficient CuV2O6 prepared via co-precipitation method. Solid State Ionics 176(29):2243–2249. https://doi.org/10.1016/j.ssi.2005.06.018
9. Li M et al (2016) "Cu3V2O8 Nanoparticles as intercalation-type anode material for lithium-ion batteries. Chem A Eur J 22(32):11405–11412. https://doi.org/10.1002/chem.201601423
10. Li G, Wu W, Zhang C, Peng H, Chen K (2010) Synthesis of ultra-long single crystalline CuV2O6 nanobelts. Mater Lett 64(7):820–823. https://doi.org/10.1016/j.matlet.2010.01.025
11. Zhang S, Peng S, Hu R, Ramakrishna S (2015) Copper vanadates/polyaniline composites as anode materials for lithium-ion batteries. RSC Adv 5(27):20692–20698. https://doi.org/10.1039/C5RA02457A
12. Sivakumar V et al (2014) Copper vanadate nanoparticles: synthesis, characterization and its electrochemical sensing property. J Mater Sci Mater Electron 25(3):1485–1491. https://doi.org/10.1007/s10854-014-1757-x
13. Camargo LP et al (2020) Copper pyrovanadate electrodes prepared by combustion synthesis: evaluation of photoelectroactivity. J Solid State Electrochem 24(8):1935–1950. https://doi.org/10.1007/s10008-020-04721-z
14. Lumley MA, Choi K-S (2017) Investigation of Pristine and (Mo, W)-doped Cu11V6O26 for use as photoanodes for solar water splitting. Chem Mater 29(21):9472–9479. https://doi.org/10.1021/acs.chemmater.7b03587
15. Kim M-W et al (2017) Electrosprayed copper hexaoxodivanadate (CuV2O6) and pyrovanadate (Cu2V2O7) photoanodes for efficient solar water splitting. J Alloys Compd 708:444–450. https://doi.org/10.1016/j.jallcom.2017.02.302
16. Gadiyar C, Strach M, Schouwink P, Loiudice A, Buonsanti R (2018) Chemical transformations at the nanoscale: nanocrystal-seeded synthesis of β-Cu2V2O7 with enhanced photoconversion efficiencies. Chem Sci 9(25):5658–5665. https://doi.org/10.1039/C8SC01314D
17. Hossain MK et al (2019) Rapid one-pot synthesis and photoelectrochemical properties of copper vanadates. ACS Appl Energy Mater 2(4):2837–2847. https://doi.org/10.1021/acsaem.9b00179
18. Jiang C-M et al (2018) Composition-dependent functionality of copper vanadate photoanodes. ACS Appl Mater Interfaces 10(13):10627–10633. https://doi.org/10.1021/acsami.8b02977
19. Rajeshwar K, Hossain MK, Macaluso RT, Janaky C, Varga A, Kulesza PJ (2018) Review-copper oxide-based ternary and quaternary oxides: where solid-state chemistry meets photoelectrochemistry (in English). J. Electrochem Soc 165(4):H3192–H3206. https://doi.org/10.1149/2.0271804jes
20. Vasil'ev AN et al (1999) Short-range and long-range magnetic ordering in alpha-CuV2O6, (in English). Phys Rev B 60(5):3021–3024. https://doi.org/10.1103/PhysRevB.60.3021

21. Vasil'ev AN et al (2000) Short-range and long-range magnetic ordering in alpha-CuV2O6, (in English). Physica B 284:1615–1616. https://doi.org/10.1016/s0921-4526(99)02720-9
22. Prokofiev AV, Kremer RK, Assmus W (2001) Crystal growth and magnetic properties of alpha-CuV2O6, (in English). J Cryst Growth 231(4):498–505. https://doi.org/10.1016/s0022-0248(01)01511-1
23. Devi RN, Rabu P, Golub VO, O'Connor CJ, Zubieta J (2002) Ligand influences on the structures of copper(II) vanadates. Structures and magnetic properties of Cu-3(triazolate)(2)V4O12 Cu-2(tpyrpyz)(2)V4O12 (tpyrpyz=tetrapyridylpyrazine) and Cu-2(pyrazine)V4O12 (in English). Solid State Sci 4(8):1095–1102. https://doi.org/10.1016/s1293-2558(02)01359-6
24. Rogado N, Haas MK, Lawes G, Huse DA, Ramirez AP, Cava RJ (2003) beta-Cu3V2O8: magnetic ordering in a spin-1/2 Kagome-staircase lattice (in English). J Phys-Condes Matter 15(6):907–914. https://doi.org/10.1088/0953-8984/15/6/317
25. He ZZ et al (2011) Unusually large magnetic anisotropy in a CuO-based semiconductor Cu5V2O10, (in English). J Am Chem Soc 133(5):1298–1300. https://doi.org/10.1021/ja110394j
26. Jezierski A (2016) Magnetic properties and stability of Cu3V2O8 compound in the different phases, (in English). J Magn Magn Mater 417:56–61. https://doi.org/10.1016/j.jmmm.2016.05.054
27. Bano K, Mittal SK, Singh PP, Kaushal S (2021) Sunlight driven photocatalytic degradation of organic pollutants using a MnV2O6/BiVO4 heterojunction: mechanistic perception and degradation pathways, (in English). Nanoscale Adv 3(22):6446–6458. https://doi.org/10.1039/d1na00499a
28. Yan S, Cai ZL, Wu D, Yu YL, Huang SL, Cao Y (2021) Z-scheme interface modification by MnV2O6 for V2O5/g-C3N4 heterostructure towards efficient visible photocatalytic activity, (in English). J Alloys Compd 882(8):160751. https://doi.org/10.1016/j.jallcom.2021.160751
29. Ben Yahia H, Gaudin E, Boulahya K, Darriet J, Son WJ, Whangbo MH (2010) Synthesis and characterization of the crystal structure and magnetic properties of the ternary manganese vanadate NaMnVO4, (in English). Inorg Chem 49(18):8578–8582. https://doi.org/10.1021/ic101180h
30. Hneda ML, da Cunha JBM, Gusmao MA, Neto SRO, Rodriguez-Carvajal J, Isnard O (2017) Low-dimensional magnetic properties of orthorhombic MnV2O6: a non-standard structure stabilized at high pressure (in English). Phys Rev B 95(2):024419. https://doi.org/10.1103/PhysRevB.95.024419
31. Garlea VO, McGuire MA, Sanjeewa LD, Pajerowski DM, Ye F, Kolis JW (2018) The magnetic order of a manganese vanadate system with two-dimensional striped triangular lattice, (in English). AIP Adv 8(10):101407. https://doi.org/10.1063/1.5043124
32. Pellizzeri TMS, McGuire MA, McMillen CD, Wen YM, Chumanov G, Kolis JW (2018) Two halide-containing cesium manganese vanadates: synthesis, characterization, and magnetic properties, (in English). Dalton Trans 47(8):2619–2627. https://doi.org/10.1039/c7dt04642a
33. Khamaru N et al (2020) Structural and magnetic investigations on Cu-doped MnV2O6 compound: Experiment and theory (in English). J Magn Magn Mater 49710:165995. https://doi.org/10.1016/j.jmmm.2019.165995
34. Ma H, Zhang S, Ji W, Tao Z, Chen J (2008) α-CuV2O6 Nanowires: Hydrothermal Synthesis and Primary Lithium Battery Application. J Am Chem Soc 130(15):5361–5367. https://doi.org/10.1021/ja800109u
35. Lafontaine MA, Le Bail A, Férey G (1990) Copper-containing minerals—I. Cu3V2O7(OH)2, 2H2O: The synthetichomolog of volborthite; crystal structure determination from X-ray and neutron data; structural correlations. J Solid State Chem 85(2):220–227. https://doi.org/10.1016/S0022-4596(05)80078-7
36. Liang Y, Liu P, Li HB, Yang GW (2012) Synthesis and characterization of copper vanadate nanostructures via electrochemistry assisted laser ablation in liquid and the optical multi-absorptions performance. Cryst Eng Comm 14(9):3291–3296. https://doi.org/10.1039/C2CE06347F
37. Bentrup U, Martin A, Wolf G-U (2003) Comparative study of the thermal and redox behaviour of alkali-promoted V2O5 catalysts. Thermochim Acta 398(1):131–143. https://doi.org/10.1016/S0040-6031(02)00334-9
38. Valmalette JC, Gavarri JR (1998) High efficiency thermochromic VO2(R) resulting from the irreversible transformation of VO2(B). Mater Sci Eng B 54(3):168–173. https://doi.org/10.1016/S0921-5107(98)00148-2
39. Zhang W, Shi L, Tang K, Liu Z (2012) Synthesis, surface group modification of 3D MnV2O6 nanostructures and adsorption effect on Rhodamine B. Mater Res Bull 47(7):1725–1733. https://doi.org/10.1016/j.materresbull.2012.03.038
40. Wu X, Wu W, Cui X, Liao S (2012) Selective self-assembly synthesis of MnV2O6·4H2O with controlled morphologies and study on its thermal decomposition. J Therm Anal Calorim 109(1):163–169. https://doi.org/10.1007/s10973-011-1577-7
41. Frost RL et al (2011) A Raman spectroscopic study of the different vanadate groups in solid-state compounds—model case: mineral phases vésigniéite [BaCu3(VO4)2(OH)2] and volborthite [Cu3V2O7(OH)2·2H2O]. J Raman Spectrosc 42(8):1701–1710. https://doi.org/10.1002/jrs.2906
42. Pan A et al (2010) Facile synthesized nanorod structured vanadium pentoxide for high-rate lithium batteries. J Mater Chem 20(41):9193–9199. https://doi.org/10.1039/C0JM01306D
43. Ghiyasiyan-Arani M, Masjedi-Arani M, Ghanbari D, Bagheri S, Salavati-Niasari M (2016) Novel chemical synthesis and characterization of copper pyrovanadate nanoparticles and its influence on the flame retardancy of polymeric nanocomposites. Sci Rep 6(1):1–9. https://doi.org/10.1038/srep25231
44. Fang YANG, Tian-hao JI, Hai-yan DU, Jia-yue SUN, Qing-lin YANG, Guang-lu G (2009) Preparation and characterization of Cu3V2O7(OH)2·2H2O hollow spheres from Na2V6O16·3H2O nanobelts. Chem Res Chin Univ 25(2):132–137

45. Benko F, Koffyberg F (2011) Semiconductivity and optical interband transitions of CuV2O6 and Cu2V2O7. Canadian J Phys 70:99–103. https://doi.org/10.1139/p92-011
46. Hassanien AS, Akl AA (2015) Influence of composition on optical and dispersion parameters of thermally evaporated non-crystalline Cd50S50−xSex thin films. J Alloys and Compd 648:280–290. https://doi.org/10.1016/j.jallcom.2015.06.231
47. Barnes G, Gentle I (2011) Interfacial science: an introduction. Oxford University Press
48. Groen JC, Peffer LAA, J. Pérez-Ramírez, (2003) Pore size determination in modified micro- and mesoporous materials. Pitfalls and limitations in gas adsorption data analysis. Microporous Mesoporous Mater 60(1):1–17. https://doi.org/10.1016/S1387-1811(03)00339-1
49. Ruiz-Rodríguez L, Blasco T, Rodríguez-Castellón E, Nieto JML (2019) Partial oxidation of H2S to sulfur on V-Cu-O mixed oxides bronzes. Catal Today 333:237–244. https://doi.org/10.1016/j.cattod.2018.07.050
50. Khan I, Qurashi A (2017) Shape Controlled synthesis of copper vanadate platelet nanostructures, their optical band edges, and solar-driven water splitting properties. Sci Reports 7(1):14370. https://doi.org/10.1038/s41598-017-14111-7
51. Swift P (1982) Adventitious carbon—the panacea for energy referencing? Surf Interface Anal 4(2):47–51. https://doi.org/10.1002/sia.740040204
52. Miller DJ, Biesinger MC, McIntyre NS (2002) Interactions of CO2 and CO at fractional atmosphere pressures with iron and iron oxide surfaces: one possible mechanism for surface contamination? Surf Interface Anal 33(4):299–305. https://doi.org/10.1002/sia.1188
53. Ghijsen et al (1988) Electronic structure of Cu2O and CuO. Phys Rev B Condens Matter 38(16):11322–11330
54. Rozier P, Galy J, Chelkowska G, Koo HJ, Whangbo MH (2002) Electrical resistivity, magnetic susceptibility X-ray photoelectron spectroscopy and electronic band structure studies of Cu2.33−xV4O11. J Solid State Chem 166(2):382–388. https://doi.org/10.1006/jssc.2002.9609
55. Eapen AK, Thomas P (2019) The novel synthesis and luminescence studies of CuO and Fe2O3 embedded (8-hydroxyquinoline)zinc nanocomposites. Turk J Phys 43:324–336. https://doi.org/10.3906/fiz-1807-39
56. van Embden J, Tachibana Y (2012) Synthesis and characterisation of famatinite copper antimony sulfide nanocrystals. J Mater Chem 22(23):11466–11469. https://doi.org/10.1039/C2JM32094K
57. Moses Ezhil Raj A et al (2010) XRD and XPS characterization of mixed valence Mn3O4 hausmannite thin films prepared by chemical spray pyrolysis technique. Appl Surf Sci 256(9):2920–2926. https://doi.org/10.1016/j.apsusc.2009.11.051
58. Ramírez A, Hillebrand P, Stellmach D, May MM, Bogdanoff P, Fiechter S (2014) Evaluation of MnOx Mn2O3 and Mn3O4 electrodeposited films for the oxygen evolution reaction of water. J Phys Chem C 118(26):14073–14081. https://doi.org/10.1021/jp500939d
59. Silversmit G, Depla D, Poelman H, Marin GB, De Gryse R (2004) Determination of the V2p XPS binding energies for different vanadium oxidation states (V5+ to V0+). J Electron Spectrosc Relat Phenom 135(2):167–175. https://doi.org/10.1016/j.elspec.2004.03.004
60. Silversmit G, Depla D, Poelman H, Marin GB, De Gryse R (2006) An XPS study on the surface reduction of V2O5(001) induced by Ar+ ion bombardment. Surf Sci 600(17):3512–3517. https://doi.org/10.1016/j.susc.2006.07.006
61. Biesinger MC, Lau LWM, Gerson AR, Smart RSC (2010) Resolving surface chemical states in XPS analysis of first row transition metals, oxides and hydroxides: Sc, Ti, V, Cu and Zn. Appl Surf Sci 257(3):887–898. https://doi.org/10.1016/j.apsusc.2010.07.086
62. Mendialdua J, Casanova R, Barbaux Y (1995) XPS studies of V2O5, V6O13, VO2 and V2O3. J Electron Spectrosc Relat Phenom 71(3):249–261. https://doi.org/10.1016/0368-2048(94)02291-7
63. Jiménez VM, Fernández A, Espinós JP, González-Elipe AR (1995) The state of the oxygen at the surface of polycrystalline cobalt oxide. J Electron Spectrosc Relat Phenom 71(1):61–71. https://doi.org/10.1016/0368-2048(94)02238-0
64. Zhou Z et al (2008) Electronic structure studies of the spinel CoFe2O4 by X-ray photoelectron spectroscopy. Appl Surf Sci 254(21):6972–6975. https://doi.org/10.1016/j.apsusc.2008.05.067
65. Mickevičius S et al (2006) Investigation of epitaxial LaNiO3−x thin films by high-energy XPS. J Alloys Compd 423(1):107–111. https://doi.org/10.1016/j.jallcom.2005.12.038
66. Köseoğlu Y (2013) Structural, magnetic, electrical and dielectric properties of MnxNi1−xFe2O4 spinel nanoferrites prepared by PEG assisted hydrothermal method. Ceramics Int 39(4):4221–4230. https://doi.org/10.1016/j.ceramint.2012.11.004
67. Mohseni H, Shokrollahi H, Sharifi I, Gheisari K (2012) Magnetic and structural studies of the Mn-doped Mg–Zn ferrite nanoparticles synthesized by the glycine nitrate process. J Magn Magn Mater 324(22):3741–3747. https://doi.org/10.1016/j.jmmm.2012.06.009